JM RAPIDS

Nonlinear regimes of tsunami waves generated by a granular collapse

Wladimir Sarlin[1], Cyprien Morize[1],†, Alban Sauret[2] and Philippe Gondret[1]

[1]Université Paris-Saclay, CNRS, Laboratoire FAST, 91405 Orsay, France

[2]Department of Mechanical Engineering, University of California, Santa Barbara, CA 93106, USA

Tsunami waves induced by landslides are a threat to human activities and safety along coastal areas. In this paper, we characterize experimentally the waves generated by the gravity-driven collapse of a dry granular column into water. Three nonlinear wave regimes are identified depending on the Froude number Fr_f based on the ratio of the velocity of the advancing granular front and the velocity of linear gravity waves in shallow water: transient bores for large Fr_f, solitary waves for intermediate values of Fr_f, and nonlinear transition waves at small Fr_f. The wave amplitude relative to the water depth increases with Fr_f in the three regimes but with different nonlinear scalings, and the relative wavelength is an increasing or decreasing function of Fr_f depending on the wave regime. Two of these wave regimes are rationalized by considering that the advancing granular front acts as a vertical piston pushing the water, while the last one is found to be a transition from shallow- to deep-water conditions. The present modelling contributes to a better understanding of the rich hydrodynamics of the generated waves, with coastal risk assessment as practical applications.

Key words: solitary waves, surface gravity waves, avalanches

1. Introduction

In 2018, the partial flank collapse of Anak Krakatau led to a tsunami that caused major human casualties and material damage along the neighbouring coast (Grilli *et al.* 2019; Paris *et al.* 2020). Many other volcanic islands are susceptible to a similar collapse with an associated risk of tsunamis, such as La Réunion in the Indian Ocean (Kelfoun, Giachetti & Labazuy 2010) or La Palma in the Atlantic Ocean (Abadie *et al.* 2012). The generation of tsunami waves by landslides may be triggered by volcanic or seismic events not only in the ocean, but also in lakes or rivers (Kremer, Simpson & Girardclos 2012; Couston, Mei & Alam 2015), due to the collapse or avalanche of either soil, rocks, or even ice and snow (Zitti *et al.* 2016). The experimental and numerical studies of Clous & Abadie (2019)

† Email address for correspondence: cyprien.morize@universite-paris-saclay.fr

and Cabrera *et al.* (2020) have recently shown that subaerial landslides trigger much larger waves than submarine landslides for a given amount of destabilized materials.

For subaerial events, the Froude number, corresponding to the ratio of the velocity of the landslide entering into the water to the wave velocity, is expected to play a crucial role. The simplest approach to model the generation of a tsunami wave by a landslide is to consider the impact of a sliding wedge on an inclined plane (Walder *et al.* 2003). However, granular materials must be considered to account for the complex landslide motion and interplay with the water. By studying the entry of grains into water at high velocity from a pneumatically launched box along a smooth inclined plane, Fritz, Hager & Minor (2004) observed different wave regimes depending on the Froude number Fr and slide thickness S: (i) transient (breaking) bores at high Fr and S; (ii) solitary-like waves at moderate Fr and S; (iii) nonlinear transition waves at low Fr and S; and (iv) weakly nonlinear oscillatory waves at very low Fr and S. Robbe-Saule *et al.* (2017) have considered the experimental gravity-driven collapse of a subaerial granular column into water. They have shown that the aspect ratio and the volume of the granular column both play an important role on the amplitude of the wave generated. With a similar but larger set-up, Huang *et al.* (2020) observed the first three wave regimes reported by Fritz *et al.* (2004), again depending on the aspect ratio and volume of the column. Recently, Robbe-Saule *et al.* (2021) have shown that the local Froude number Fr_f based on the horizontal velocity v_f of the granular front at the water surface is the relevant parameter that governs the generation of the wave. However, a theoretical framework that accounts for the different wave regimes observed experimentally remains elusive. This lack of knowledge makes difficult the development of accurate predictive models and coastal risk assessment in the context of tsunamis generated by landslides, which is one of the grand challenges in environmental fluid mechanics (Dauxois *et al.* 2021).

In this paper, we report experimental results of the wave generated by a gravity-driven granular collapse into water for a large range of local Froude number Fr_f, and characterize the three wave regimes observed: (i) transient bore waves at high Fr_f; (ii) solitary waves at intermediate Fr_f; and (iii) nonlinear transition waves at small Fr_f. For the first two regimes, theoretical models from the shallow-water wave equations are then developed, which compare well to the experimental results.

2. Experimental set-up and results

2.1. *Set-up*

We perform new experiments using the two-dimensional set-up illustrated in figure 1(*a*) and described in detail in Robbe-Saule *et al.* (2021). A rectangular tank of length $L = 2$ m and transverse width $W = 0.15$ m is filled up to a height h_0 with initially still water. On the left-hand side of the tank, a rectangular granular column of height H_0 and length L_0 stands on a solid step of height h_0 so that the grains, initially retained by a vertical gate, are just above the water interface. The granular material consists of monodisperse glass beads of diameter 5 mm and density $\rho = 2.5$ g cm^{-3}. Images are taken by a camera from the sidewall of the tank. The water is dyed with fluorescein to enhance the contrast and facilitate the processing of the time evolution of the free surface of the water and of the grains.

At time $t = 0$, the gate is quickly lifted by a linear motor at 1 m s^{-1}. The granular column then collapses into the water, leading to an advancing granular front $x_f(t)$, which generates an impulse wave of amplitude $A(t)$ and mid-height width $\lambda(t)$, as sketched in figure 1(*b*). We perform systematic experiments, where both the size of the column and the water depth
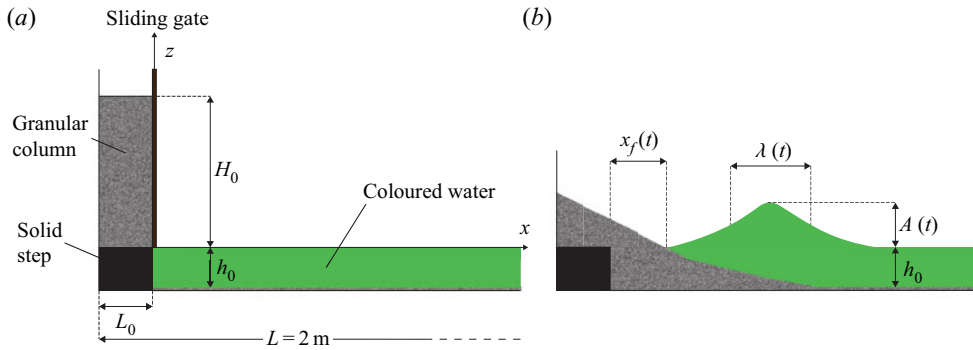
(*a*) Sliding gate   (*b*)

Figure 1. Sketch of the experimental set-up (*a*) in the initial configuration, with a dry granular column of height H_0 and length L_0 above a water depth h_0, and (*b*) during the granular collapse, with an advancing front $x_f(t)$ at the water surface and a generated wave of amplitude $A(t)$ and mid-height width $\lambda(t)$.

H_0 (cm)	L_0 (cm)	V_0 (dm^3)	a	h_0 (cm)	Fr_0	Symbols
9	10	1.35	0.9	2–25	0.6–2.1	■
19	10	2.85	1.9	2–25	0.9–3.1	●
29	10	4.35	2.9	2–20	1.2–3.8	▲
39	5	2.93	7.8	2–25	1.2–4.4	▼
39	10	5.85	3.9	2–20	1.4–4.4	★
39	14.5	8.48	2.7	2–20	1.4–4.4	◆
39	20	11.7	2.0	2–20	1.2–4.4	▶

Table 1. Sets of experimental parameters with corresponding data symbols.

are varied, as detailed in table 1. We explore a large range of aspect ratio $a = H_0/L_0$, initial volume of the column $V_0 = H_0 L_0 W$, and global Froude number $Fr_0 = \sqrt{H_0/h_0}$, which compares the typical vertical free-fall velocity of the granular medium, $\sqrt{gH_0}$, to the velocity of linear gravity waves in shallow water, $c_0 = \sqrt{gh_0}$.

2.2. *Description of the observed regimes of nonlinear waves*

Depending on the geometry of the granular columns and the water depth, leading to different global Froude number Fr_0, we observe three different regimes of nonlinear waves (see figure 2(*a–c*), and supplementary movies available at https://doi.org/10.1017/jfm. 2021.400). At large Fr_0, strong asymmetric waves are generated with the shape of transient positive surges or bores, as shown in figure 2(*a*). The wave generated systematically breaks in the near-field region, and corresponds to the plunging breaker reported in Robbe-Saule *et al.* (2021). At moderate Fr_0, quasi-symmetrical waves are generated, consisting of a unique main pulse of soliton-like shape, as reported in figure 2(*b*). This wave may break or not depending on its relative amplitude A/h_0. The breaking cases at high A/h_0 correspond to spilling breakers (Robbe-Saule *et al.* 2021). At low Fr_0, waves with slightly reversed asymmetry and strong unsteadiness are generated (see figure 2*c*). This situation corresponds to the nonlinear transition waves reported by Fritz *et al.* (2004) and Viroulet *et al.* (2013).

    Figure 2(*d–f*) report the time evolution of the granular collapse and of the generated wave for the three examples of figure 2(*a–c*). At high Fr_0 (grey ◇), the position of the
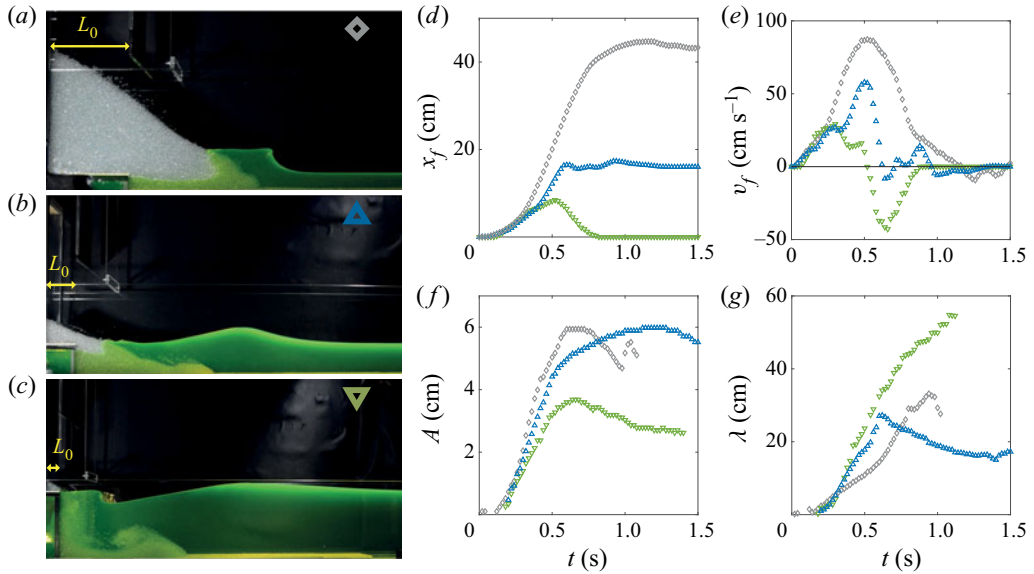
Figure 2. (*a*–*c*) Photographs of the different wave shapes observed: (*a*) bore wave at $H_0 = 39$ cm, $L_0 = 14.5$ cm, $h_0 = 4$ cm ($Fr_0 = 3.1$, $Fr_f = 1.39$); (*b*) solitary wave at $H_0 = 29$ cm, $L_0 = 10$ cm, $h_0 = 8$ cm ($Fr_0 = 1.9$, $Fr_f = 0.65$); and (*c*) nonlinear transition wave at $H_0 = 39$ cm, $L_0 = 5$ cm, $h_0 = 25$ cm ($Fr_0 = 1.2$, $Fr_f = 0.19$). (*d*–*g*) Time series of (*d*) the position x_f and (*e*) the velocity v_f of the granular front, and of (*f*) the amplitude A and (*g*) the mid-height width λ of the wave for the experiments of panels (*a*) grey $\diamond$, (*b*) blue $\triangle$, and (*c*) green $\triangledown$.

granular front, $x_f(t)$, continually increases from zero to a final maximum value $x_{f_\infty} \gg h_0$ ($x_{f_\infty} \simeq 11h_0$ in figure 2*d*). The corresponding velocity of the front $v_f = \mathrm{d}x_f/\mathrm{d}t$ exhibits a bell shape from zero up to a maximum value $v_{f_m} \gtrsim \sqrt{gh_0}$ ($v_{f_m} \simeq 1.4\sqrt{gh_0}$ in figure 2*e*) and then decreases to zero. Both the amplitude A and the mid-height width λ increase during the generation process, until reaching a maximum value $A_m \gtrsim h_0$ with the corresponding $\lambda_m \gg h_0$ ($A_m \simeq 1.5h_0$ and $\lambda_m \simeq 5h_0$ in figure 2*f*,*g*, respectively), at the moment where the plunging breakup occurs ($t \simeq 0.7$ s in figure 2*e*), which leads to a sudden decrease of A.

At moderate Fr_0 (blue $\triangle$), the time evolution of the granular collapse is similar to that described above but with a smaller maximal extension $x_{f_\infty} \gtrsim h_0$ and a smaller maximum velocity $v_{f_m} \simeq \sqrt{gh_0}$ ($x_{f_\infty} \simeq 2h_0$ and $v_{f_m} \simeq 0.7\sqrt{gh_0}$ in figure 2*d*,*e*, respectively). The wave amplitude increases abruptly first and then more slowly to a maximum value $A_m \simeq h_0$ ($A_m \simeq 0.75h_0$ in figure 2*f*) before decreasing due to the breaking of the wave. In the meantime, the width λ first grows up to a maximum value, and then decreases down to $\lambda_m > h_0$ ($\lambda_m \simeq 3h_0$ in figure 2*f*) when the wave propagates away from the collapse.

At low Fr_0 (green $\triangledown$), the time evolution of the granular collapse is very different from the two previous situations: x_f increases from zero up to a maximum value $x_{f_m} \lesssim h_0$ ($x_{f_m} \simeq 0.3h_0$ in figure 2*d*) before decreasing down to zero when the flow rate of the granular medium starts to vanish. In this configuration, the bottom wall does not play a significant role in the granular dynamics. The corresponding velocity $v_f(t)$ exhibits first a positive maximum $v_{f_m} < \sqrt{gh_0}$ ($v_{f_m} \simeq 0.2\sqrt{gh_0}$ in figure 2*e*), but also a negative minimum at the end of the collapse, corresponding to the receding phase of the granular flow. In the meantime, while the wave amplitude first increases to a maximum value $A_m < h_0$ before slightly decreasing, the mid-height width displays a monotonic growth beyond $\lambda_m \simeq h_0$ ($A_m \simeq 0.3h_0$ and $\lambda_m \simeq 1.2h_0$ in figure 2*f*,*g*, respectively), revealing that the wave
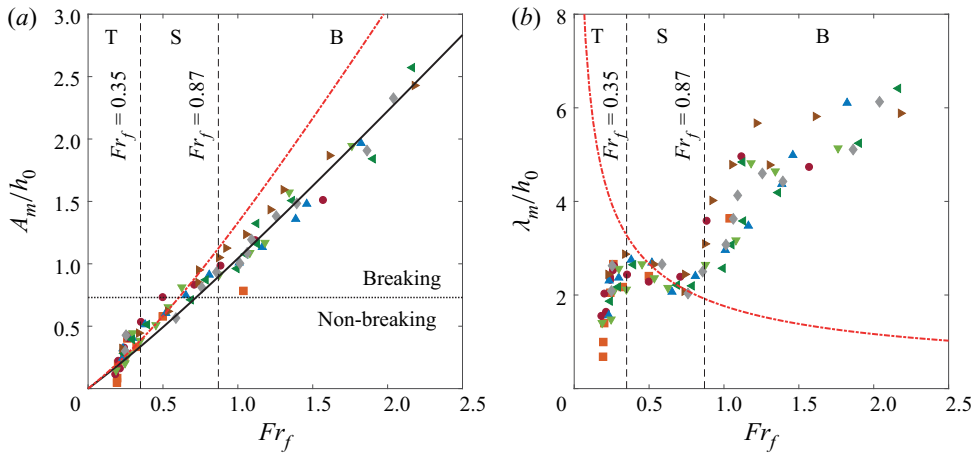
919 R6-4

Figure 3. (a) Relative amplitude A_m/h_0 and (b) mid-height width λ_m/h_0 of the generated waves as functions of the local Froude number Fr_f for all the experiments of table 1, with predictions from (3.3) (black full line) and (3.9) (red dashed line). The two vertical thin dashed lines at $Fr_f = 0.35$ and $Fr_f = 0.87$ separate the three regimes corresponding to nonlinear transition waves (T), solitary waves (S) and bore waves (B), respectively. The horizontal dotted line at $A_m/h_0 \simeq 0.73$ separates breaking and non-breaking waves.

flattens after its generation. These waves all exhibit a wavelength much larger than the capillary length $\lambda_c \simeq 1.6$ cm and larger than the water depth (except for a few experiments that are discussed in § 3.3), so that they correspond to gravity waves in shallow-water conditions.

The local Froude number, $Fr_f = v_{f_m}/\sqrt{gh_0}$, based on the velocity of the granular front, was found to be the relevant dimensionless parameter to describe the wave generation (Robbe-Saule *et al.* 2021). All the experimental results for the maximum wave amplitude A_m and the associated mid-height width λ_m, non-dimensionalized by the water depth h_0, are plotted as a function of Fr_f in figure 3(*a,b*). A monotonic increase of the relative wave amplitude A_m/h_0 with Fr_f is observed, whereas the relative mid-height width λ_m/h_0 first increases but then slightly decreases before increasing again. These different behaviours lead to a clear separation of the three wave regimes described above: nonlinear transition waves (T) for $Fr_f \lesssim 0.35$, solitary waves (S) for $0.35 \lesssim Fr_f \lesssim 0.87$, and transient bore waves (B) for $Fr_f \gtrsim 0.87$. In the next section, we characterize the wave regimes using theoretical models adapted to the different regimes and obtain scaling laws for the maximal wave amplitude and the corresponding wavelength with the local Froude number Fr_f, for regimes S and B.

3. Modelling the generation of the different nonlinear waves

3.1. *Bore waves*

For large values of Fr_f (regime B, $Fr_f \gtrsim 0.87$), the deformation of the free surface of the water is very similar to a bore or a positive surge during the generation process: the shape is an elongated water bump of height $h_0 + A_B$ with an abrupt step front propagating over the downstream region of height h_0. These waves are observed during the collapse of granular columns with a large initial height H_0 relative to the water depth h_0, and therefore for large Fr_0. In such conditions, the advancing granular front is almost vertical throughout the entire water depth and acts as a vertical translating piston over a distance $x \gg h_0$ at the velocity v_p (see figure 2a). We consider the mass and momentum conservation equations
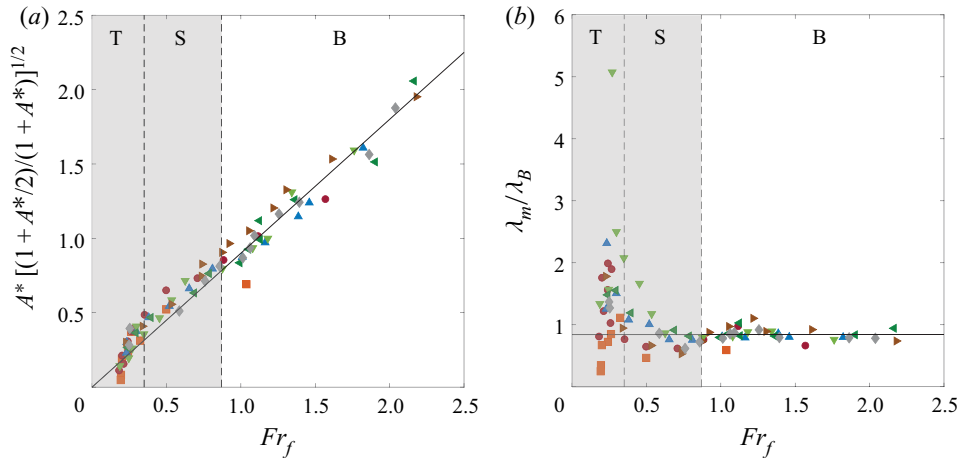
Figure 4. (a) Plot of $A^*[(1 + A^*/2)/(1 + A^*)]^{1/2}$ as a function of Fr_f for all the experimental data of table 1, with $A^* = A_m/h_0$, and the best linear fit (full line) with a slope 0.9 for the data corresponding to bore waves ($Fr_f \gtrsim 0.87$). (b) Ratio of the experimental mid-height width λ_m of the wave to the calculated one, λ_B, from (3.4), as a function of Fr_f. The horizontal solid line corresponds to $\lambda_m/\lambda_B = 0.84$.

in the frame of reference of the bore propagating at the velocity c:

$$\left.\begin{array}{c}(c - v_p)(h_0 + A_B) - ch_0 = 0, \\ (c - v_p)^2(h_0 + A_B) - c^2h_0 + \frac{g}{2}[(h_0 + A_B)^2 - h_0{}^2] = 0.\end{array}\right\} \quad (3.1)$$

These equations describe a stationary hydraulic jump of amplitude A_B, separating a thin supercritical region of depth h_0 and constant velocity $-c$ from a thick subcritical region of depth $h_0 + A_B$ and of constant velocity $v_p - c$, when assuming no dissipation at the bottom wall and a hydrostatic vertical pressure gradient far enough from the jump (Guyon *et al.* 2015). Combining these two equations leads to a nonlinear relation between the relative amplitude A_B/h_0 and the Froude number $Fr_p = v_p/\sqrt{gh_0}$ based on the piston velocity v_p:

$$\frac{A_B}{h_0}\left(\frac{1 + A_B/(2h_0)}{1 + A_B/h_0}\right)^{1/2} = Fr_p. \quad (3.2)$$

Figure 4(a) shows the rescaled experimental data using the left-hand side of (3.2), with $A_B = A_m$, as a function of Fr_f. The data corresponding to $Fr_f \gtrsim 0.87$ collapse onto a straight line of slope 0.9. Therefore, these nonlinear waves can be seen as bores generated by a solid wall pushing the water at an effective constant velocity v_p, a little smaller than the maximal velocity of the granular front v_{f_m}. The explicit expression for A_B/h_0 as a function of Fr_p can be obtained as the only positive solution of the third-order equation (3.2):

$$\frac{A_B}{h_0} = \frac{2}{3}\left\{2\sqrt{1 + 3Fr_p{}^2/2}\cos\left(\frac{1}{3}\cos^{-1}\left[\frac{3}{4}\frac{(Fr_p - 2\sqrt{2}/3)(Fr_p + 2\sqrt{2}/3)}{(Fr_p{}^2 + 2/3)\sqrt{1 + 3Fr_p{}^2/2}}\right]\right) - 1\right\}. \quad (3.3)$$

The solid line in figure 3(a) corresponds to (3.3) with $Fr_p = 0.9Fr_f$. This prediction fits very well the data for $Fr_f \gtrsim 0.87$, i.e. in regime B. Note that this nonlinear variation

919 R6-6

would asymptotically tend to the linear expression $A_B/h_0 \sim \sqrt{2}Fr_p$ as $Fr_p \to +\infty$. The wavelength λ_B can also be estimated from the mass conservation at the end of the generation of the bore, assuming that the hydraulic jump has the shape of a pure step. Indeed, when the piston has travelled over the total distance x_p, we should have

$$\lambda_B = x_p \frac{h_0}{A_B}. \tag{3.4}$$

Figure 4(b) presents the ratio λ_m/λ_B as a function of Fr_f. Here, we consider that x_p corresponds to the value of x_f at the end of the wave generation, when $A = A_m$. A plateau is observed with a value $\lambda_m/\lambda_B \simeq 0.84$ for $Fr_f \gtrsim 0.87$. Since the hydraulic jump is not a pure step and the granular front is not exactly a vertical advancing wall at a constant velocity, the observed wavelength λ_m is indeed a little smaller than the predicted value λ_B. Note that (3.4) implies that $\lambda_B/h_0 \sim (x_p/h_0)Fr_f^{-1}$ at large Fr_f, where λ_B/h_0 depends not only on Fr_f but also on x_p/h_0. This explains why the experimental data λ_m/h_0 of regime B do not collapse onto a master curve in figure 3(b), but are quite dispersed, as they also depend on x_{f_m}/h_0.

3.2. Solitary waves

In an intermediate range of local Froude number (regime S, $0.35 \lesssim Fr_f \lesssim 0.87$), the generated waves exhibit a solitary-like shape. Solitons are solutions of the Korteweg–de Vries equation valid for shallow-water waves without dissipation (Dauxois & Peyrard 2006). In that theoretical framework, the free surface elevation $\eta(x, t)$ of a soliton is given by

$$\eta(x, t) = A_S \operatorname{sech}^2 \left(\frac{c_S t - x}{\lambda_S} \right), \tag{3.5a}$$

with

$$\lambda_S = 2h_0 \sqrt{\frac{h_0}{3A_S}} \quad \text{and} \quad c_S = \sqrt{gh_0} \left(1 + \frac{A_S}{2h_0} \right), \tag{3.5b,c}$$

where A_S, λ_S and c_S are the amplitude, characteristic width and velocity of the wave, respectively, and sech is the hyperbolic secant function. These solitons can be generated experimentally by wavemakers with a vertical piston moving according to the following law (Goring & Raichlen 1980; Synolakis 1990; Guizien & Barthélemy 2002):

$$x_p(t) = \frac{A_S \lambda_S}{h_0} \tanh \left(\frac{c_S t - x_p(t)}{\lambda_S} \right). \tag{3.6}$$

Note that, for the experiments in this regime, the time evolution of the granular front $x_f(t)$ is close to a hyperbolic tangent evolution, as shown by the curve in figure 2(d). The maximum value of the time derivative of (3.6) leads to the following equation for the maximum velocity v_p of the piston:

$$v_p = \frac{A_S}{h_0} (c_S - v_p). \tag{3.7}$$

Considering the expression (3.5c) for c_S together with (3.7) leads to a relation between the relative wave amplitude of the solitary wave A_S/h_0 and the Froude number Fr_p based on the piston velocity v_p:

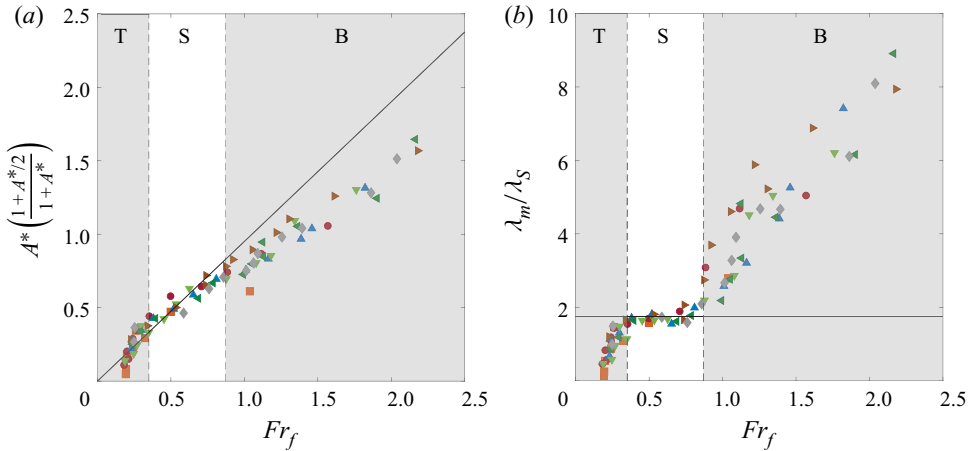$$\frac{A_S}{h_0} \frac{1 + A_S/(2h_0)}{1 + A_S/h_0} = Fr_p. \tag{3.8}$$

919 R6-7

Figure 5. (a) Plot of $A^*[(1 + A^*/2)/(1 + A^*)]$ as a function of Fr_f for all experiments, with $A^* = A_m/h_0$. The best linear fit (full line) of slope 0.95 for the data corresponding to the solitary wave regime ($0.35 \lesssim Fr_f \lesssim 0.87$) is also shown. (b) Plot of λ_m/λ_S as a function of Fr_f, with the expected plateau value $\lambda_m/\lambda_S = 1.76$ (horizontal full line).

Figure 5(a) shows the rescaled experimental data using the left-hand side of (3.8), with $A_S = A_m$, as a function of Fr_f. All the experimental data for $0.35 \lesssim Fr_f \lesssim 0.87$ collapse well onto a straight line of slope 0.95. Therefore, in the corresponding experiments, the advancing granular front acts as a moving piston with an effective maximal velocity $v_{f_m} = 0.95\, v_p$. This value is a little smaller than one, which may come from the fact that the granular front is not solid but porous and not perfectly vertical. The explicit expression for A_S/h_0 as a function of Fr_p is obtained as the only positive solution of the second-order equation (3.8):

$$\frac{A_S}{h_0} = Fr_p + \sqrt{1 + Fr_p^2} - 1. \tag{3.9}$$

The red dashed curve in figure 3(a) corresponds to (3.9) with $Fr_p = 0.95Fr_f$, and fits well the data for $0.35 \lesssim Fr_f \lesssim 0.87$. The exact expression (3.9) can be approximated, using Taylor series, by $A_S/h_0 = Fr_p + Fr_p^2/2$, which differs by less than 4 % up to $Fr_p \simeq 0.87$. Note that the expected transition from solitary waves to bores can simply be inferred from the intercept of the approximate law $A_S/h_0 = Fr_p + Fr_p^2/2$ for solitons with the approximate linear law $A_B/h_0 \simeq \sqrt{2}Fr_p$ for bores. Considering $A_S = A_B$, by continuity, leads to the critical Froude number $Fr_{p_c} = 2(\sqrt{2} - 1) \simeq 0.8$ and thus to the critical local Froude number $Fr_{f_c} \simeq 2(\sqrt{2} - 1)/0.9 \simeq 0.9$. This value corresponds well to the observed transition value of $Fr_f \simeq 0.87$. Figure 5(b) reports the ratio of the experimental mid-height width λ_m relative to the expected length λ_S obtained from (3.5). We observe a clear plateau value $\lambda_m/\lambda_S \simeq 1.8$ for $0.35 \lesssim Fr_f \lesssim 0.87$, in agreement with the expected value $2\cosh^{-1}(\sqrt{2}) \simeq 1.76$. This further confirms that the waves observed in regime S correspond to solitary waves. The red dashed curve in figure 3(b), corresponding to the theoretical prediction obtained by combining (3.5b) and (3.9), fits well the data with $Fr_p \simeq 0.95Fr_f$, and can be approximated by $2\cosh^{-1}(\sqrt{2})\lambda_S/h_0 \simeq 2.03(1 - Fr_p/2)Fr_p^{-1/2}$. In this regime of solitary waves, the relative width λ_m/h_0 of the wave decreases for increasing Fr_f, in contrast with the other wave regimes, which makes possible a clear differentiation between them. Hence, while (3.3) and (3.9) give almost the same predictions for the
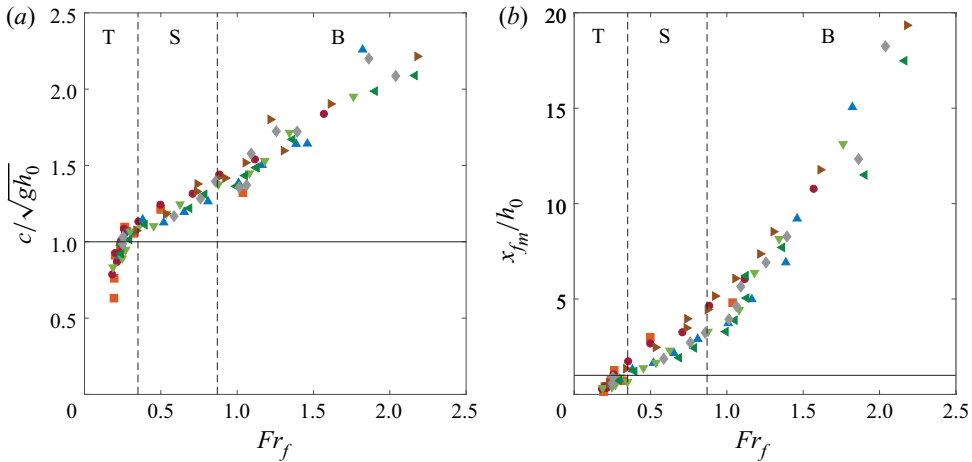
919 R6-8

Figure 6. (*a*) Evolution of $c/\sqrt{gh_0}$ with Fr_f, where the horizontal full line emphasizes a ratio value of one. (*b*) Plot of x_{f_m}/h_0 as a function of Fr_f, where the horizontal full line shows a ratio value of one.

relative amplitude in regime S, as observed in figure 3(*a*), only the solitary wave model estimates correctly the width of the waves in this regime. From these observations, we conclude that solitary waves are generated for a narrow range of Fr_f, where the granular collapse acts as a piston wavemaker with variable velocity. Note that these solitary waves are not stable but break for $Fr_f \gtrsim 0.60$, corresponding to $A_m/h_0 \gtrsim 0.73$, not far from the critical value 0.78 predicted by Tanaka (1986).

3.3. *Nonlinear transition waves*

For small values of the local Froude number (regime T, with $Fr_f \lesssim 0.35$), the waves are characterized by strong unsteadiness (wave flattening after generation), and the presence of a dispersive minor wave train. These waves recall one of those observed by Viroulet *et al.* (2013) and correspond to the nonlinear transition waves reported by Fritz *et al.* (2004). Figure 3 shows that both the amplitude and wavelength of the generated waves vary abruptly at $Fr_f \simeq 0.2$. Hence the local Froude number Fr_f, based on the horizontal velocity of the granular front relative to the velocity of shallow-water waves, is not the relevant parameter in regime T any more, for two reasons. First, the shallow-water condition begins to break down in this regime, as observed in figure 6(*a*), where the evolution of the dimensionless wave velocity $c/\sqrt{gh_0}$ is reported as a function of Fr_f. While $c/\sqrt{gh_0} > 1$ when $Fr_f \gtrsim 0.35$ for regimes S and B, $c/\sqrt{gh_0}$ decreases abruptly below one when $Fr_f \lesssim 0.35$ in regime T. Second, in figure 6(*b*), where the maximum horizontal extension of the granular front x_{f_m}, made dimensionless with the water depth h_0, is reported as a function of Fr_f, we observe that $x_{f_m}/h_0 > 1$ when $Fr_f \gtrsim 0.35$ for regimes S and B, whereas $x_{f_m}/h_0 < 1$ when $Fr_f \lesssim 0.35$ for regime T. In this last regime, x_f may not be the only relevant parameter encoding the initial perturbation that generates the wave. This could be the vertical extension y_f of the granular collapse just below the water surface or a combination of y_f and x_f. Hence, regime T corresponds to a transition from shallow- to deep-water conditions, for which developing a theoretical framework is challenging. Note that, for deep-water conditions, all the parameters characterizing both the granular collapse (x_f and v_f) and the generated waves (A_m and λ_m) are not expected to depend on h_0 any more. In that case, wave generation would be related to the Cauchy–Poisson

problem, where a surface impulse generates a modulated wave train (Stoker 1957), which may correspond to the fourth regime of weakly nonlinear oscillatory waves mentioned by Fritz *et al.* (2004).

4. Conclusion

In this study, we reported three different regimes of nonlinear surface waves generated by the gravity-driven collapse of a granular column into water, depending on the local Froude number Fr_f based on the velocity of the advancing granular front at the water surface. Transient bore waves are observed at high Fr_f where the granular front acts as a vertical piston pushing the water over the entire water depth and along a distance much larger than h_0, at a constant velocity. Solitary waves are observed when Fr_f is moderate, where the granular front also acts as a vertical piston, but with a varying velocity pushing water along a smaller distance. The amplitude and the mid-height width of the wave generated in these two strongly nonlinear regimes are captured by models derived from shallow-water equations. A third regime corresponding to nonlinear transition waves is observed at low Fr_f, which corresponds to a transition from shallow- to deep-water conditions. In this regime, the local Froude number is no longer the relevant parameter to describe the amplitude and the mid-height width of the wave, and a different model should be developed in future studies. It would also be interesting to provide a better understanding of the dynamics of the grains entering into water in this complex situation (Saingier, Sauret & Jop 2021), to develop a fully predictive model from the initial granular column to the generated waves.

Author ORCIDs.

Ⓓ Wladimir Sarlin https://orcid.org/0000-0002-2668-2279;

Ⓓ Cyprien Morize https://orcid.org/0000-0002-6966-648X;

Ⓓ Alban Sauret https://orcid.org/0000-0001-7874-5983;

Ⓓ Philippe Gondret https://orcid.org/0000-0002-7184-9429.

REFERENCES

ABADIE, S.M., HARRIS, J.C., GRILLI, S.T. & FABRE, R. 2012 Numerical modeling of tsunami waves generated by the flank collapse of the Cumbre Vieja Volcano (La Palma, Canary Islands): tsunami source and near field effects. *J. Geophys. Res.* **117**, C05030.

CABRERA, M.A.., PINZON, G., TAKE, W.A. & MULLIGAN, R.P. 2020 Wave generation across a continuum of landslide conditions from the collapse of partially submerged to fully submerged granular columns. *J. Geophys. Res.* **125** (12), 020JC016465.

CLOUS, L. & ABADIE, S. 2019 Simulation of energy transfers in waves generated by granular slides. *Landslides* **16** (9), 1663–1679.

COUSTON, L.-A., MEI, C.C. & ALAM, M.-R. 2015 Landslide tsunamis in lakes. *J. Fluid Mech.* **772**, 784–804.

DAUXOIS, T., *et al.* 2021 Confronting grand challenges in environmental fluid mechanics. *Phys. Rev. Fluids* **6** (2), 020501.

DAUXOIS, T. & PEYRARD, M. 2006 *Physics of Solitons*. Cambridge University Press.

FRITZ, H., HAGER, W. & MINOR, H. 2004 Near field characteristics of landslide generated impulse waves. *ASCE J. Waterway Port Coastal Ocean Engng* **130**, 287–302.

GORING, D.G. & RAICHLEN, F. 1980 The generation of long waves in the laboratory. In *Proceedings 17th Coastal Engineering Conference*, pp. 763–783. ASCE.

GRILLI, S.T., *et al.* 2019 Modelling of the tsunami from the december 22, 2018 lateral collapse of Anak Krakatau volcano in the Sunda Straits, Indonesia. *Sci. Rep.* **9**, 11946.

GUIZIEN, K. & BARTHÉLEMY, E. 2002 Accuracy of solitary wave generation by a piston wave maker. *J. Hydraul. Res.* **40** (3), 321–331.

GUYON, E., HULIN, J.-P., PETIT, L. & MITESCU, C.D. 2015 *Physical Hydrodynamics*. Oxford University Press.

HUANG, B., ZHANG, Q., WANG, J., LUO, C., CHEN, X. & CHEN, L. 2020 Experimental study on impulse waves generated by gravitational collapse of rectangular granular piles. *Phys. Fluids* **32** (3), 033301.

KELFOUN, K., GIACHETTI, T. & LABAZUY, P. 2010 Landslide-generated tsunamis at réunion island. *J. Geophys. Res.* **115**, F04012.

KREMER, K., SIMPSON, G. & GIRARDCLOS, S. 2012 Giant Lake Geneva tsunami in AD 563. *Nat. Geosci.* **5** (11), 756.

PARIS, A., HEINRICH, P., PARIS, R. & ABADIE, S. 2020 The december 22, 2018 Anak Krakatau, Indonesia, landslide and tsunami: preliminary modeling results. *Pure Appl. Geophys.* **177** (2), 571–590.

ROBBE-SAULE, M., MORIZE, C., BERTHO, Y., SAURET, A. & GONDRET, P. 2017 Experimental study of wave generation by a granular collapse. *EPJ Web Conf.* **140**, 14007.

ROBBE-SAULE, M., MORIZE, C., HENAFF, R., BERTHO, Y., SAURET, A. & GONDRET, P. 2021 Experimental investigation of tsunami waves generated by granular collapse into water. *J. Fluid Mech.* **907**, A11.

SAINGIER, G., SAURET, A. & JOP, P. 2021 Falling jet of dry granular material in water. *J. Fluid Mech.* **916**, A34.

STOKER, J.J. 1957 *Water Waves: The Mathematical Theory with Applications*, pp. 156–163. Interscience Publishers.

SYNOLAKIS, C. 1990 Generation of long waves in laboratory. *ASCE J. Waterway Port Coastal Ocean Engng* **116** (2), 252–266.

TANAKA, M. 1986 The stability of solitary waves. *Phys. Fluids* **29** (3), 650–655.

VIROULET, S., CÉBRON, D., KIMMOUN, O. & KHARIF, C. 2013 Shallow water waves generated by subaerial solid landslides. *Geophys. J. Intl* **193**, 747–762.

WALDER, J.S., WATTS, P., SORENSEN, O.E. & JANSSEN, K. 2003 Tsunamis generated by subaerial mass flows. *J. Geophys. Res.* **108** (B5), 2236.

ZITTI, G., ANCEY, C., POSTACCHINI, M. & BROCCHINI, M. 2016 Impulse waves generated by snow avalanches: momentum and energy transfer to a water body. *J. Geophys. Res.* **121** (12), 2399–2423.